



Thermomechanical Analysis of A-TIG and MP-TIG Welding of 2.25Cr-1Mo Steel Considering Phase Transformation

A.R. Pavan, B. Arivazhagan, M. Zubairuddin, S. Mahadevan, and M. Vasudevan

(Submitted May 1, 2018; in revised form May 7, 2019; published online August 5, 2019)

In the present study, a finite element-based 3D mesh model is used to simulate the effect of welding processes on the temperature distribution, residual stress and distortion in 11-mm-thick 2.25Cr-1Mo steel weld joints. Tungsten inert gas (TIG) and activated-TIG (A-TIG) welding processes were employed for the fabrication of weld joints. Austenite-to-bainite phase transformation is taken into account in the numerical analysis. The heat input fitting tool has been used to calibrate the heat source by matching the simulated weld bead with that of the actual weld bead. Peak temperature was higher at the weld center for A-TIG weld joint, and the weld joint exhibited a sharp temperature gradient at the weld interface. There was good agreement between the predicted and measured thermal cycles. A-TIG and multipass-TIG (MP-TIG) weld joints exhibited similar longitudinal residual stresses in heat affected zone with a difference of 50 MPa. Moreover, A-TIG weld joint fabricated by double-side welding technique employing two passes exhibited reduced distortion than MP-TIG weld joints. A higher magnitude of distortion was in MP-TIG weld joint which was attributed to more weld metal volume caused by more number of weld passes required to fill the V-groove. There was good agreement between the predicted and measured residual stress and distortion values.

Keywords 2.25Cr-1Mo steel, A-TIG, phase transformation, residual stress and distortion, TIG welding

1. Introduction

The 2.25Cr-1Mo (P22) steel is commonly employed as a structural material in power generation, petrochemical industries and particularly in heavy wall pressure vessels (Ref 1, 2). Generally, P22 is fabricated into tubes, thick-walled pipes and headers used in the operating temperature higher than 550 °C. Since the structural designs during fabrication involve welding, the integrity of weld joints is of utmost importance.

The quality of the weld joints depends on the joint efficiency and welding process being used. Hence, for joining of P22 steel, TIG welding is the most commonly used welding process (Ref 3). TIG welding provides high-quality weld joints which are less susceptible to hot corrosion (Ref 4). However, welding of thicker materials (above 3 mm) involves joint preparation and requires the use of filler metal. To resolve this problem, A-TIG welding has been employed to enhance the penetration depth autogenously in single welding pass. The activated flux made of a mixture of metallic oxides is applied over the joint in the form of a paste prior to the welding. The oxygen from the

flux enters the molten weld pool causing a change in the convective flow and thereby increases the depth of penetration during welding (Ref 5-7). A-TIG produces good-quality joint as compared to MP-TIG welding (Ref 8, 9).

However, residual stress is commonly seen near the weld joints due to localized heating and cooling and is inevitable (Ref 10-12). Tensile residual stresses can considerably influence the properties of structural components. Notably, it can reduce the fatigue life, dimensional stability, corrosion resistance, increase the distortion and promote the brittle fracture. Shrinkage of molten weld metal during welding accompanying the solid-state phase transformation has a significant role in generating the tensile residual stress near the vicinity of the weld joint. Further, considering the solid-state phase transformation for the prediction of welding residual stress using numerical simulation is more challenging (Ref 13). Also, a number of numerical models have been proposed in P22 steel weld joint in order to predict accurately and understand the evolution of welding residual stress and distortion (Ref 14-18).

Moreover, very limited literature has considered the solid-state phase transformation effect in P22 steel weld joint (Ref 14, 17). Deng et al. (Ref 14) investigated the effects of solid-state phase transformations on welding residual stress in a multipass butt-welded P22 steel pipes by developing a finite element method (FEM). The author considered the JMAK equation to describe the austenite-to-bainite phase transformation and Koistinen-Marburger relationship for martensitic transformation. In addition, they studied the change in welding residual stress due to the volumetric change by phase transformation and change in yield strength. This eventually showed a significant effect on the residual stress in the P22 steel pipe. However, the research on understanding the thermomechanical behavior of A-TIG weld is limited (Ref 8, 19). It is

A.R. Pavan and M. Vasudevan, Homi Bhabha National Institute, Mumbai, India; and Metallurgy and Materials Group, Indira Gandhi Centre for Atomic Research, Kalpakkam, India; B. Arivazhagan and S. Mahadevan, Metallurgy and Materials Group, Indira Gandhi Centre for Atomic Research, Kalpakkam, India; and M. Zubairuddin, Homi Bhabha National Institute, Mumbai, India. Contact e-mail: dev@igcar.gov.in.

well understood from the various literatures that A-TIG welding provides excellent joint property with reduced residual stress and distortion as compared to MP-TIG welding (Ref 8, 9). Moreover, the level of residual stress and distortion during A-TIG welding of P22 steel was not yet explored.

In this work, the P22 steel weld joint was fabricated using MP-TIG welding and the A-TIG welding processes. The thermomechanical behavior of both the weld joints was studied using finite element modeling employing SYSWELD to deduce the evolution of residual stress and distortion. The simulated results were validated with the experimental measurements.

2. Research Methodology

The research methodology followed in this work is described in the form of flow sheet in Fig. 1. The thermomechanical analysis of A-TIG and MP-TIG weld joints was carried out using FEM and validated with experimental results. In the numerical simulation, initially transient temperature was calculated and sequentially coupled to the mechanical analysis to achieve residual stress and distortion.

2.1 Finite Element Modeling

The dimensions of the plate are $300 \times 120 \times 11 \text{ mm}^3$. For MP-TIG welding process, butt joint configuration with 70° groove angle was used, and for A-TIG welding process, a straight-sided configuration was used (without any groove). Numerical simulations of both the weld joints were performed using commercial software SYSWELD V. 2015 (developed by ESI group, France) (Ref 20). The optimization of mesh size or

the right choice of mesh dimensions is required for improving the accuracy of simulations (Ref 21). Therefore, to capture the exact experimental condition in the numerical model, the optimized element dimension during meshing is necessary. During welding simulation, the effect of temperature and flux gradient is more near the fusion zone and heat affected zone. In the present work, around 30 mm near to the weld line, a fine mesh with a size of $1 \text{ mm} \times 0.8 \text{ mm}$ (quadrilateral) was chosen. For A-TIG welding, the model was simulated in two welding passes without any filler metal deposition (157,185—nodes, 143,160—elements) as shown in Fig. 2(a). On the other hand, for MP-TIG welding, a model with V-groove was simulated with 15 number of weld passes (137,378—nodes, 132,936—elements) as shown in Fig. 2(b).

Goldak double-ellipsoidal heat source model (Ref 22) was utilized for the moving heat source. Thermomechanical analysis is done by sequential coupling of thermal and mechanical analysis, where the heat transfer analysis was followed by mechanical analysis. Hence, the thermal strains computed from temperature differences relative to the initial part temperature and phase transformation strains obtained from the nonlinear heat transfer analysis are fed to the nonlinear mechanical analysis to calculate the mechanical effect on the weld joint. It was assumed that there is no influence of any structural changes on the thermal analysis part.

2.1.1 Material Properties. The residual stresses originate in weld joints mainly due to change in thermophysical, mechanical properties and microstructural characteristics of materials to be welded. Thus, for the accurate prediction of the weld-induced residual stress and distortion, it is mandatory to choose appropriate material properties. The material database was created for P22 steel using material database manager tool.

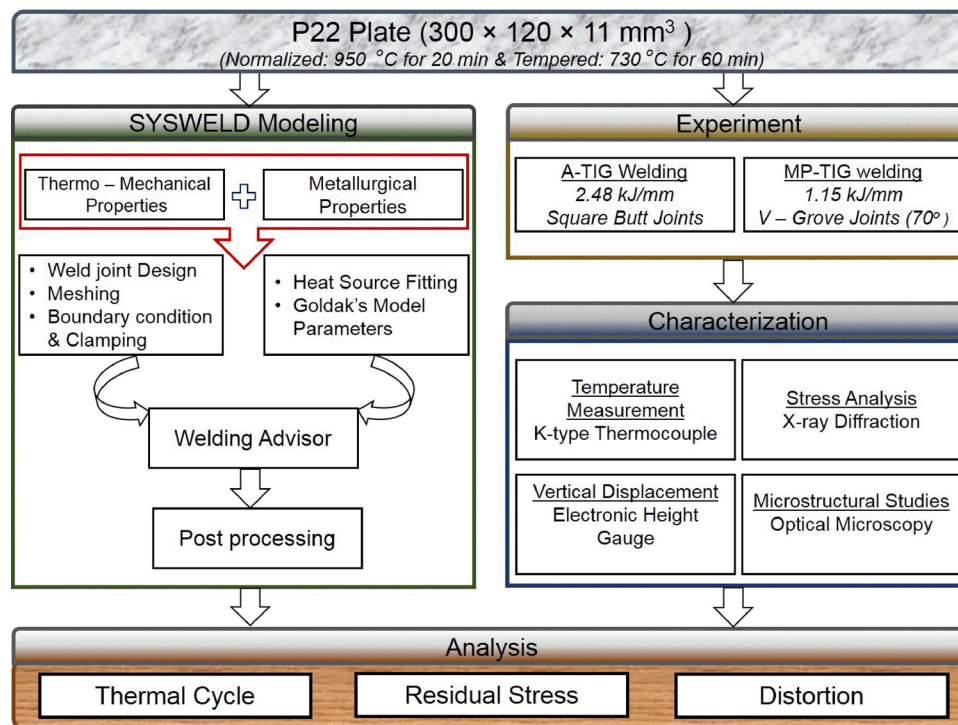


Fig. 1 Research summary in flow sheet

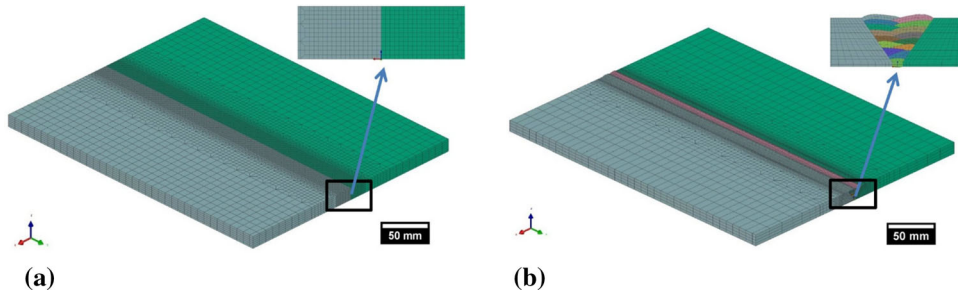


Fig. 2 Model of (a) A-TIG and (b) MP-TIG weld joints

All material properties for each phase to account for phase transformation are taken from 10CrMo9-10 present in SYSWELD Richter database, while yield strength values were taken from the literature (Ref 14, 23) as shown in Fig. 3(a). It is necessary to consider the heat transfer effect due to fluid flow behavior in the molten pool. Hence, to account for heat transfer caused by fluid flow in molten metal, the thermal conductivity value was increased to 2-3 times above the melting temperature in the analysis.

2.1.2 Governing Equations. The heat transfer due to localized heating during welding is primarily due to conduction mode. Heat conduction in the material can be described by using the Fourier law of heat conduction as shown in the following equation:

$$\nabla(k\nabla T) + Q = \rho C(\partial T/\partial t) \quad (\text{Eq 1})$$

where ρ is the density (kg/m^3), C is the specific heat ($\text{J/kg } ^\circ\text{C}$), k is the thermal conductivity ($\text{W/m } ^\circ\text{C}$) and Q is the volumetric heat flux (W/m^3).

The rate of convection and the radiation heat transfer is governed by Newton's law of cooling and Stefan-Boltzmann law, respectively, as shown in Eq 2 and 3:

$$Q_c - h_c(T_s - T_o) = 0 \quad (\text{Eq 2})$$

$$Q_r - \varepsilon\sigma(T_s^4 - T_o^4) = 0 \quad (\text{Eq 3})$$

where h_c is film coefficient for convection [$\sim 25 \text{ W/(m}^2 \text{ K)}$], σ —Stefan-Boltzmann constant ($5.67 \times 10^{-8} \text{ W/m}^2 \text{ K}^4$), ε —emissivity (0.8), T_s —surface temperature (K) and T_o —ambient temperature (K).

For considering phase transformation from the parent phase to austenite transformation in the analysis, Leblond's equation was used (Ref 24). Also, for diffusion-controlled transformations (austenitic, ferritic, pearlitic and bainitic transformations), Leblond/Johnson-Mehl-Avrami (JMA) law was used (Eq 4). Leblond's law is the simplest approach, mainly for continuous heating or cooling transformations. Moreover, JMA law is a more generalized (in comparison with Leblond) approach for isothermal and continuous heating or cooling transformations:

$$p = 1 - \exp(-kt^n) \quad (\text{Eq 4})$$

where p is the volume fraction of bainite, t is time and k and n are kinetic parameters. The parameters of the JMA equation should be extracted from the continuous cooling transformation (CCT) diagram. The CCT diagram for P22 steel was not available in SYSWELD database. Thus, a CCT diagram of comparable material, 2Cr-0.5Mo steel, is chosen as shown in

Fig. 3(b). Here, we have assumed in the model that there is no formation of martensite upon cooling in the weld metal.

Hence, during heating, phase transformations usually occur from

- Ferrite/pearlite \rightarrow austenite
- Bainite \rightarrow austenite

and during cooling, phase transformations usually occur from

- Austenite \rightarrow ferrite/pearlite
- Austenite \rightarrow bainite

The mechanical analysis is performed by applying the computed thermal histories. During the fusion welding process, the total strain induced on the material can be divided into elastic, thermal, plastic and due to phase transformation which can be written as follows:

$$e^{\text{total}} = e^{\text{elastic}} + e^{\text{thermal}} + e^{\text{plastic}} + e^{\text{phase}} \quad (\text{Eq 5})$$

the force equilibrium for mechanical analysis is given below:

$$\sigma_{ij} + p_j = 0 \quad (\text{Eq 6})$$

where σ_{ij} is stress tensor and p_j is body force at any point within the boundary. For the finite element formulation, the basic equilibrium equation can be used to achieve the virtual induced strain and displacement.

2.1.3 Boundary Condition. During welding, radiation heat losses dominate near the weld pool because of localized heating, while convection heat losses dominate away from the weld pool. Thus, all the surfaces were assigned to radiation loss in the model. The initial temperature was taken as $30 \text{ } ^\circ\text{C}$. During the experiment, the weld joint was clamped to avoid distortion. Similar to the experimental constraints, external constraints were assigned on the weld joint to restrain it appropriately in the model. Therefore, the rotational motion and translational motion of the weld joint were avoided in the numerical model by arresting rigid body motion. Though the model was rigid clamped, it does not mean that the component is restrained with infinite stiffness. The finite stiffness of the constraint allows it to move due to thermal expansion during differential heating. The idealized elastic clamp with a finite stiffness of 1000 N/mm is used in vertical and in-plane condition to obtain the proper deformation during the numerical simulation. The multipass weld analysis was performed by without considering the higher passes during initial pass simulation, also known as Chewing Gum method. During the

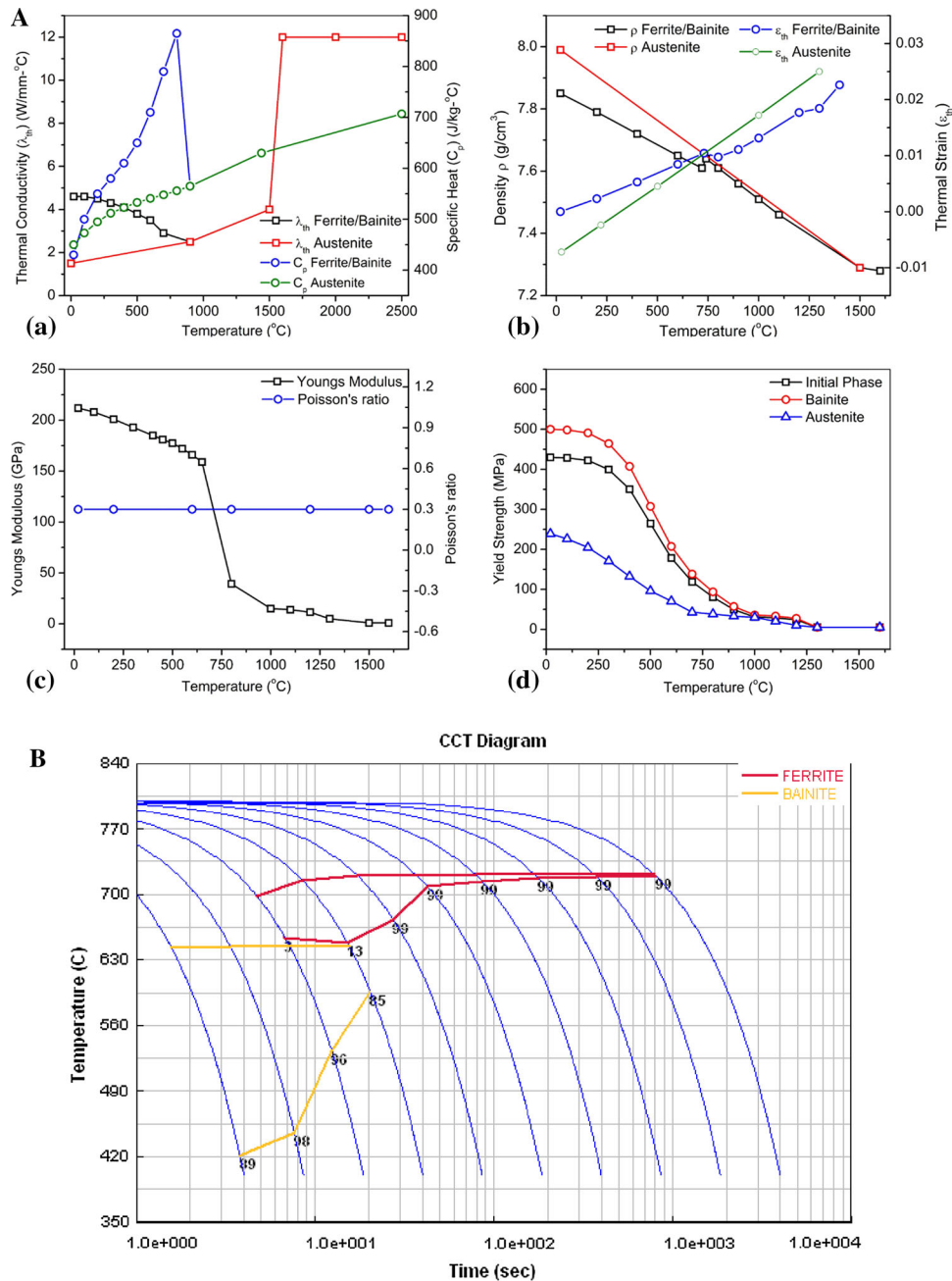


Fig. 3 (a) material properties of 2.25Cr-1Mo steel: (a) thermal conductivity and specific heat capacity, (b) density and thermal strain, (c) Young's modulus and Poisson's ratio and (d) yield strength (SYSWELD material database). (b) CCT diagram of 2Cr-0.5Mo (SYSWELD export)

simulation of the first pass, the higher bead material, in other words, dummy material is assigned to lower stiffness value, i.e., 1 N/mm. Isotropic hardening model was used to consider elastic-plastic material behavior.

2.2 Experimental

The material used in this research is P22 low-alloy steel. The as-received material in the form of plates of size 300 × 120 × 11 mm 3 in normalized and tempered conditions was used in the fabrication of weld joints. The chemical composition is shown in Table 1. The configuration of square butt and V-groove (angle 70°) joint is shown in Fig. 4(a) and (b), respectively.

In A-TIG welding, initially, multicomponent oxide flux was prepared by mixing oxide powders (for example, SiO $_2$, TiO $_2$, MoO $_3$, etc.) in acetone to form a paste/flux. Further, the prepared flux is applied over the joint surface by using a paintbrush and allowed to dry. Later, the weld pad was clamped at the four corners of the plate and finally on top of oxide flux-coated surface the A-TIG welding was performed as depicted in Fig. 4(a). However, MP-TIG weld pad was clamped using stiffeners as shown in schematic Fig. 4(b). To fill the V-groove joint, matching filler wire of diameter 2.4 mm was used. The welding process parameters are shown in Table 2. The sequence of experimental work carried out is shown in Fig. 1.

The weld joints were fabricated using A-TIG (average heat input 2.48 kJ/mm) and MP-TIG (average heat input ~ 1.15 kJ/

Table 1 Chemical composition of P22 steel (wt. %)

Material	C	Mn	Si	Cr	Mo	Ni	P	S	Cu
2.25Cr-1Mo steel	0.15	0.66	0.26	2.36	0.93	0.19	0.02	0.02	0.05

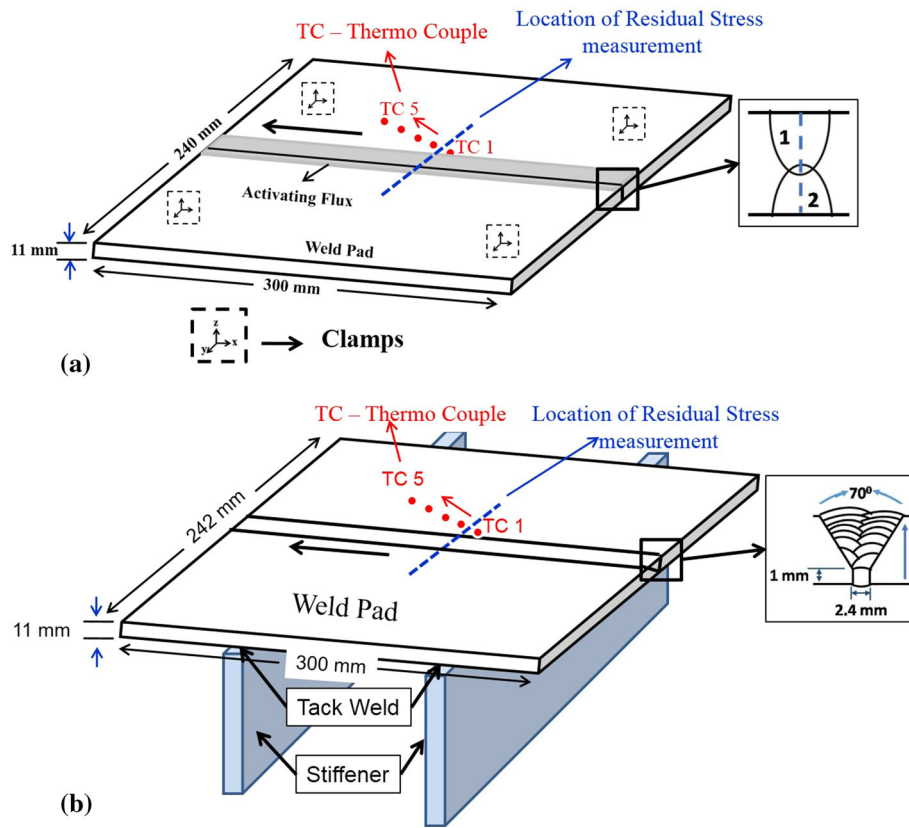


Fig. 4 Weld pad configuration of (a) A-TIG, (b) MP-TIG weld joints

Table 2 Welding process parameters

Welding process	Welding pass	Current, A	Voltage, V	Torch speed, mm/min	Heat input, kJ/mm
<i>Autogenous welding</i>					
A-TIG	1	230	15.4	60	2.479
	2	230	14.5	60	2.334
<i>Multipass tungsten inert gas welding</i>					
MP-TIG	1	110	11.85	57	0.960
	2	120	10.7	50	1.078
	3	130	11.3	50	1.233
	4	140	10.65	56	1.118
	5	140	11.35	50	1.334
	6	145	12.55	85	0.899
	7	145	12.35	60	1.253
	8	145	13.25	66	1.222
	9	145	13.2	57	1.410
	10	145	12.3	58	1.291
	11	145	12.3	59	1.269
	12	145	12.8	67	1.163
	13	145	12.5	59	1.290
	14	145	11	84	0.797
	15	145	12.55	75	1.019

mm) welding processes, respectively. The transient temperature during the welding process is captured by Chromel-Alumel thermocouples, which was spot welded over the weld joint surface. The thermocouple placement was made at 6-mm intervals in the transverse direction from the joint and 10-mm interval along the welding direction in A-TIG weld joint. However, in MP-TIG weld joint, thermocouples were spot welded at 3-mm intervals in the transverse direction from the groove edge (13 mm from the weld center) and 10-mm interval along the welding direction as shown in Fig. 4(a) and (b).

The as-welded samples were sectioned, mounted and polished for microstructural characterization. SiC sandpapers were used for grinding, and diamond suspensions (3 and 1 μm) were used for polishing. A cross-sectional specimen was extracted from the as-welded weld joint, as shown in Fig. 5.

Vickers hardness across the cross section of the polished specimen was measured with a 300 g force and a 15 s dwell time. X-ray diffraction-based welding residual stresses were calculated in the weld joint using a Rigaku MSF 2 M x-ray diffraction system with chromium $K\alpha$ radiation (2.2896 \AA). The slope of a linear plot of d-spacing versus specimen angle gives the residual strain in the material. Further, mathematically the obtained strains were converted into stresses by using the following equation:

$$\sigma_{\phi} \equiv \left(\frac{E}{1 + \nu} \right)_{(hkl)} \frac{1}{d_{\phi_0}} \left(\frac{\partial d_{\phi\psi}}{\partial \sin^2 \psi} \right) \quad (\text{Eq 7})$$

where E refers to Young's modulus, ν is Poisson's ratio and d_0 is lattice spacing at $\psi = 0$. The angle ψ can be defined as the angle between the normal of the surface and the incident and diffracted beam bisector (orientation of sample) normally varying from 0° to 45° . To measure distortion, the height of the plate was measured before and after welding at marked grid

points using vertical electronic height gauge having a least count of 0.002 mm.

3. Results and Discussion

3.1 Heat Source Fitting and Thermal Analysis

It is well understood that the amount of heat input employed for welding plays a significant role in changing the microstructure (phase transformation) as well as the mechanical properties. For thermomechanical analysis, heat source fitting (HSF) was conducted to get the best possible arc source at particular welding process efficiency. Hence, the weld macrograph was calibrated and compared with experimental results to ensure the proper supply of heat energy into the weld joint. But in MP-TIG welding, it is difficult to accurately obtain the information of individual bead shape (width/area/depth). However, the bead shape of each welding pass was modeled with actual heat input. Mainly for the TIG welding process, double-ellipsoidal heat source model (Fig. 6) was used for HSF analysis. The equation of heat source model is given below (Eq 8 and 9):

$$q_f(x, y, z, t) = \frac{6\sqrt{3}f_t Q}{a_f b c \pi \sqrt{\pi}} e^{-3x^2/a_f^2} e^{-3y^2/b^2} e^{-3[z+v(\tau-t)]^2/c^2} \quad (\text{Eq 8})$$

$$q_r(x, y, z, t) = \frac{6\sqrt{3}f_r Q}{a_r b c \pi \sqrt{\pi}} e^{-3x^2/a_r^2} e^{-3y^2/b^2} e^{-3[z+v(\tau-t)]^2/c^2} \quad (\text{Eq 9})$$

The heat input equation is given below:

$$Q = \left(\frac{I \times V \times \eta}{v} \right) \quad (\text{Eq 10})$$

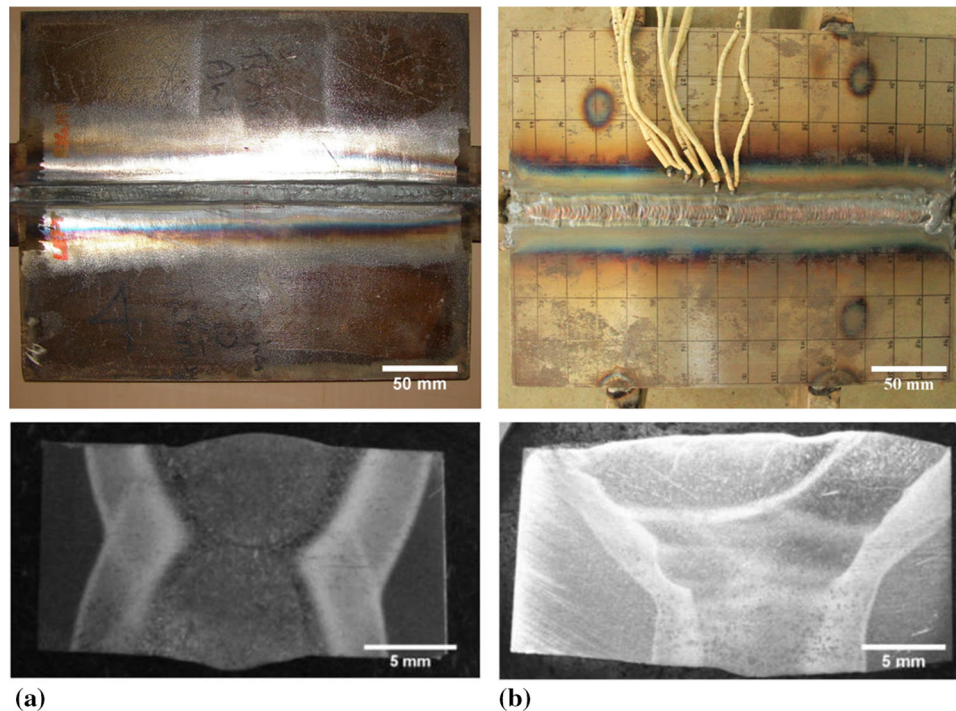


Fig. 5 Weld joints and cross section of (a) A-TIG, (b) MP-TIG weld joints

where a is the front length of the molten pool, a_r is the rear length of the molten pool, c is the depth of penetration and b is half width as shown in Table 3. The front (f) and rear (r) heat depositing factors of heat source were considered as 0.4 and 1.6, respectively. q_r and q_f are power densities in W/m^3 . V is voltage, η is the process efficiency, I is current and v is the torch velocity in mm/min.

Based on heat source fitting, predicted values of weld bead geometry such as bead width and depth were compared with measured macrographs shown in Fig. 7(a). In the case of MP-TIG, simulation results show a higher molten weld pool volume compared to the weld bead macrograph shown in Fig. 7(b). This is due to the addition of filler wire with torch weaving, but in simulation straight-line trajectory was considered. Hence, in this model, the molten weld pool volume is slightly higher.

The comparison of measured and predicted thermal cycles near the weld line is shown in Fig. 8. The first thermocouple placed near to the weld centerline for the A-TIG weld joint showed peak temperature of 1100 °C. From first to the fifth thermocouples across the weld direction showed drastic decay in the peak temperature as shown in Fig. 8(a). The decrease in temperature indicates the localized heating of an arc source, where power density was pointed at the center and spread across with respect to the center of a point source. Figure 8(b) shows the differential heating and cooling cycle of 15 weld

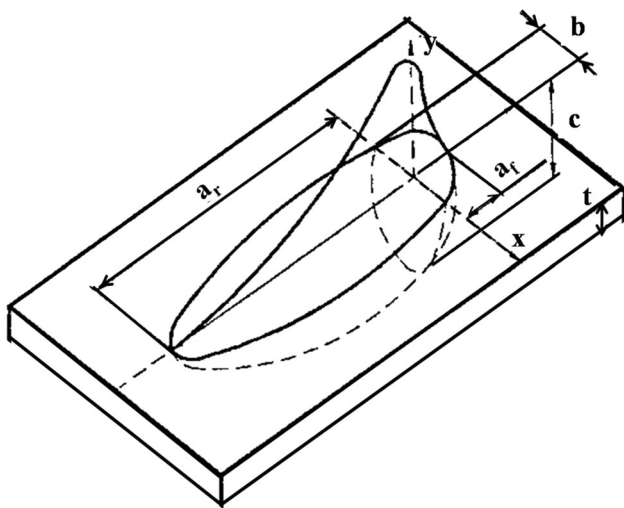


Fig. 6 Goldak's double-ellipsoidal heat distribution model

passes in MP-TIG weld joint. In MP-TIG welding, during the initial pass, all the other pass elements were deactivated and accordingly heat transfer boundary conditions were modified.

The drop in peak temperature in alternate weld pass corresponds to weld metal deposition at the right and left side of the groove. The surface is deposited alternatively for smooth solidification to reduce mechanical distortion. The P22 steel has higher thermal conductivity compared to austenitic steels. However, the temperature has increased during consecutive passes. The increase in temperature can be attributed to the continuous metal deposition, that is, one over the other without much time lag. Both predicted and experimental thermal cycles are in good agreement with each other. However, the experimental limitation to measure the temperature at the weld center can be overcome by a numerical simulation model, and the resulting thermal cycle of the first pass during A-TIG and MP-TIG welding is shown in Fig. 9(a) and (b). The red dot indicates the location of the temperature profile obtained. The decrease in peak temperature as a function of time gives the signature of higher (freshly) deposited weld passes over the first weld pass and gives information about the repeated heating and cooling observed at the weld center. The thermal cycles in Fig. 9(a) and (b) suggest that the material has undergone a phase transformation in A-TIG and in MP-TIG weld joints due to repeated heating and cooling cycles. The cooling time from 800 to 500 °C ($t_{8/5}$) of the first pass and second pass of A-TIG welding is 38.38 and 41.03 s, respectively. Almost the same cooling time was observed for both the welding passes due to the similar supply of heat input during welding. However, in MP-TIG welding, $t_{8/5}$ of first five welding passes is found to be around 9.78 s, eighth welding pass is 22.64 s and the 11th displayed 43.8 s. Here, the first few passes showed fast cooling time due to large heat sink; further, the subsequent passes exhibited relatively slower cooling time due to a decreased heat sink (built-up heat by former passes) and the supply of different welding heat inputs during welding. From the existing literature, it was understood that phase transformation depends on the cooling time of weld. Therefore, the bainitic phase can form in this range of cooling time (9.78-43.8 s) during A-TIG and MP-TIG welding, and this was observed in the microstructure of weld (Ref 25, 26). In A-TIG and MP-TIG welding simulation, the peak temperature was found to be 1606 °C and 1624 °C, respectively. Thermal cycle across the weld direction shows the sharp decrease in peak temperature (Fig. 10a), which, in turn, indicates the effect of localized heating. Figure 10(b) depicts the steady-state nature of the weld

Table 3 Heat source parameters

Goldak's double-ellipsoidal heat source distribution model					
Welding process	Welding pass	Front length a_f , mm	Rear length, a_r , mm	Half width, b , mm	Depth, c , mm
A-TIG	1	6	10	4.8	6.12
	2	6	10	5	6.78
MP-TIG	1	2	4	2	2
	2	2	4	2.4	2
	3-6	3	5	2.8	2
	7-8	4	6	3	2
	9	4	6	3.2	2
	10-13	4	6	3.4	2
	14	4	6	3.6	2
15	4	6	3.8	2	

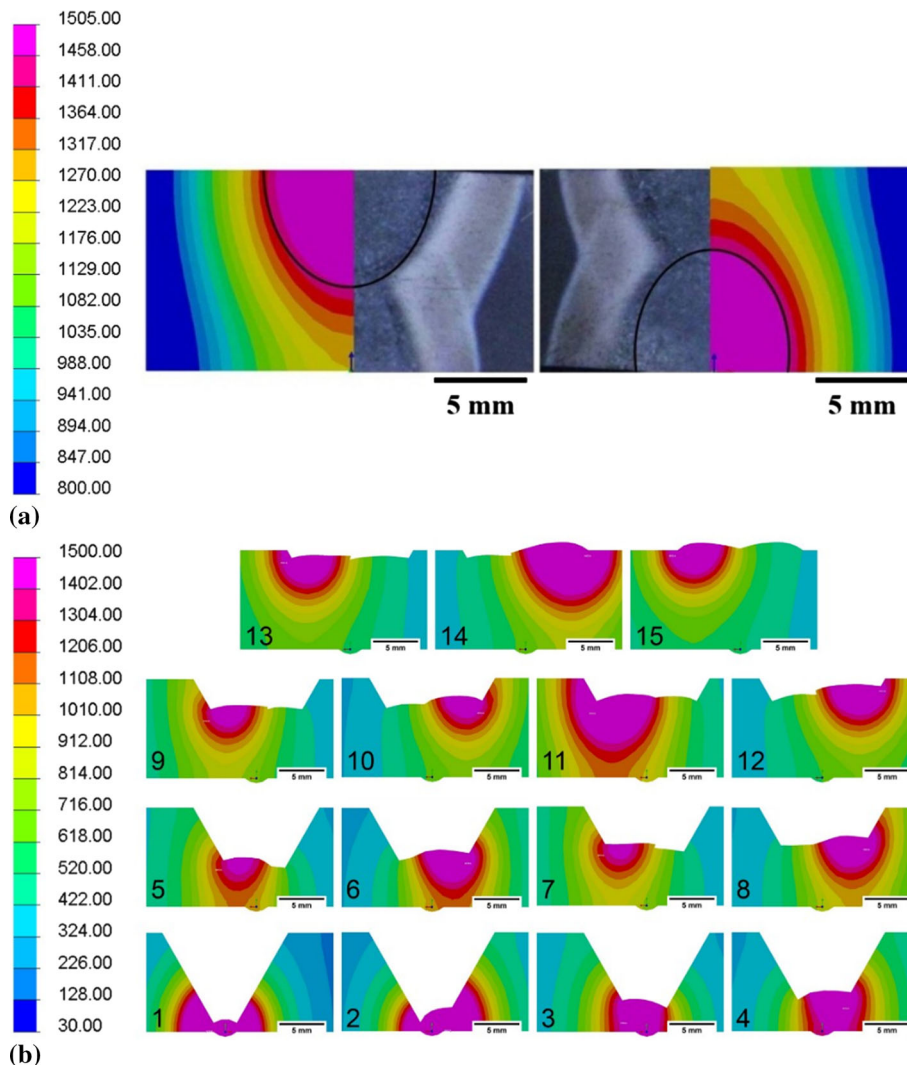


Fig. 7 Bead profile (temperature °C) of (a) A-TIG, (b) MP-TIG weld joints

thermal cycle. The shift in peak as a function of time is due to moving heat source.

3.1.1 Phase Transformation. Heating a material to its melting temperature range and cooling it down to room temperature drastically change the initial and final microstructures. During heating, the ferrite (initial) phase transforms to austenite, which, in turn, changes the crystal structure from body-centered cubic (BCC) to face-centered cubic (FCC) structure. Change in crystal structure from BCC to FCC reduces the volume. During air cooling, austenite transforms to bainite, with a corresponding increase in volume. Thermal strains and volume change occurred because phase transformation plays a dominant role in the course of residual stress generation. Also, the yield strength of the base and weld metal determines the magnitude of residual stress. Hence, the proper selection of material properties with necessary assumptions should be carefully considered to achieve a reasonable result. In order to consider the phase transformation effect in the model, JMA equation was used (Eq 4).

As the temperature starts to increase beyond A_1 (1080 °C) of P22 steel, initial phase (ferrite) starts to disappear and appear like austenite and completely transforms to austenite when the temperature reaches A_3 (1140 °C). Upon cooling as described

above, austenite transforms to bainite. The bainite start temperature varies from 490 to 520 °C for P22 steel. Also, it can be predicted by using Eq 11 (Ref 3):

$$Bs \text{ (}^\circ\text{C)} = 630 - 45Mn - 40V - 35Si - 30Cr - 25Mo - 20Ni - 15W.$$

(Eq 11)

But, in the case of numerical simulation, the bainite start (Bs) temperature was found to be at around 600 °C. Moreover, good resolution in achieving exact Bs temperature can be brought into the numerical model with the selection of proper metallurgical data inputs. Figure 11(a) and (b) shows the phase formation during heating and cooling at the same location as shown in Fig. 9(a) and (b). While heating, initial phase (ferrite/bainite) starts to transform to austenite at austenization temperature (~ 1080 °C) and becomes 100% austenite above 1200 °C. In the case of MP-TIG weld joint, filler wire activated and continuously deposited over the v-groove with particular torch velocity as defined in Table 2. Initially, the filler wire phase is assigned with parent material properties. Hence, at the austenization temperature, filler phase transforms to austenite as indicated by a dotted line. Upon cooling, the phase transfor-

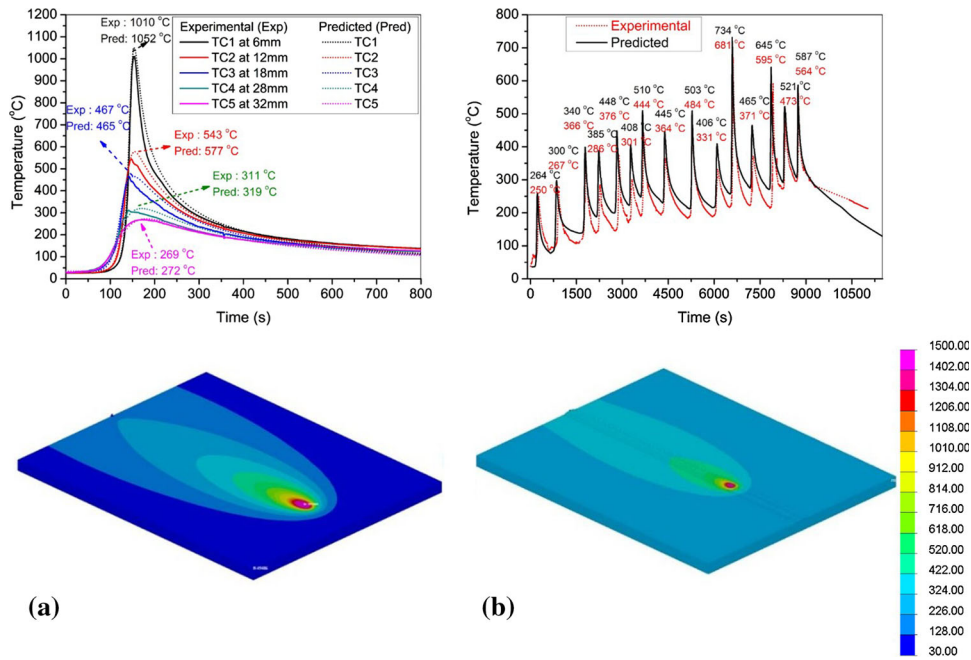


Fig. 8 Thermal cycle of (a) A-TIG, (b) MP-TIG weld joints

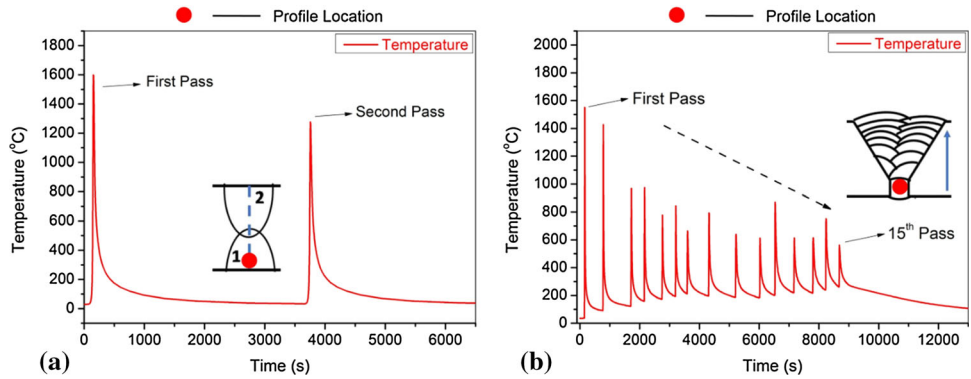


Fig. 9 Predicted thermal cycle at first weld pass of (a) A-TIG and (b) MP-TIG weld joints

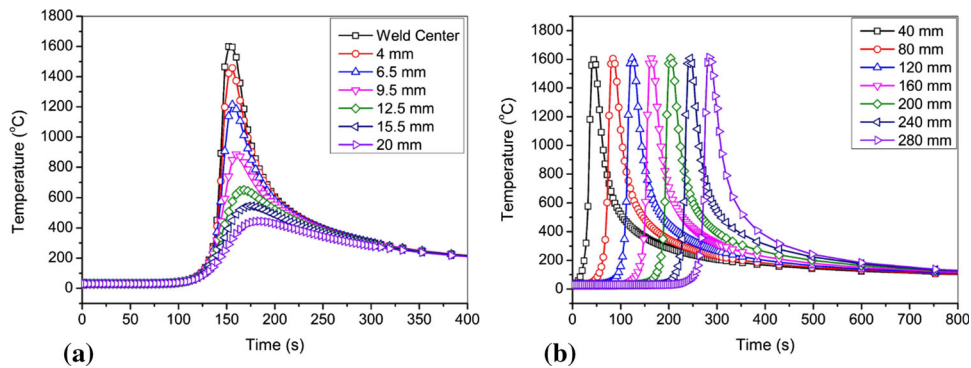


Fig. 10 A-TIG thermal cycle: (a) transverse, (b) longitudinal directions

mation occurs from austenite to bainite around 600 °C, typically known as Bs temperature. Eventually, bainitic phase transformation depletes around 460 °C and forms the bainite phase as an end product at room temperature with ~ 10 to 20%

of proeutectoid ferrite and prior austenitic phases as indicated by circles. Figure 11 shows the phase formation during heating and cooling which also agrees with the microstructure as shown in Fig. 13.

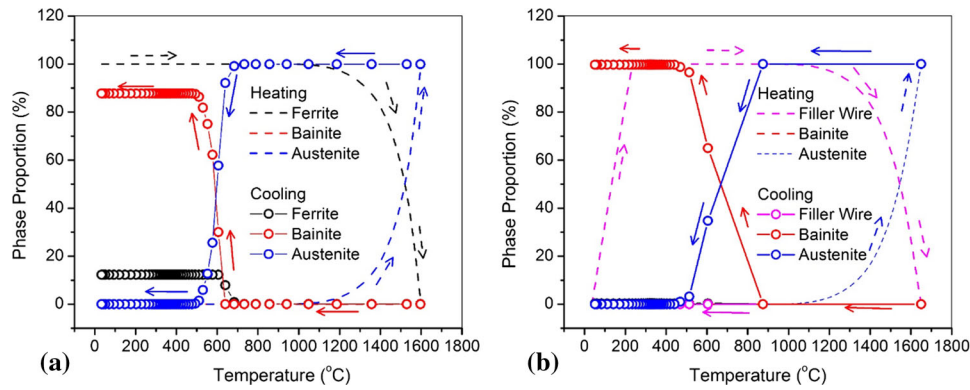


Fig. 11 Temperature-dependent phase formation in (a) A-TIG and (b) MP-TIG weld joints

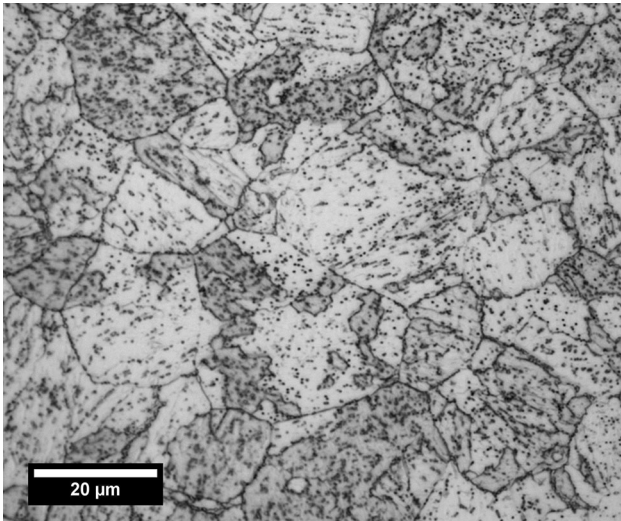


Fig. 12 Optical micrograph of as-received base metal

3.2 Microstructure and Microhardness

As-received microstructure of P22 steel is shown in Fig. 12. The mixture of granular bainitic and proeutectoid ferrite was observed with an average grain size of 14.86 μm . Also, a large number of precipitates were found on the bainitic matrix.

The weld joints fabricated by A-TIG and MP-TIG welding showed a granular bainite, ferrite phase and lath-like arrangement of ferrite and carbide, which is typically known as upper bainite, as shown in Fig. 13(a) and (b). The lath structure is not uniform; some bainitic laths were large in size. The average size of the bainitic packets was found to be 33.85 μm in A-TIG weld joint and 10.7 μm in MP-TIG weld joint. The complex thermal cycle in MP-TIG welding is that the newer pass reheats the previously deposited metal and alters the microstructure and grain size. Hence, there is a noticeable change in the bainitic lath structure and average grain size as well. Near the fusion zone, the microstructure of heat affected zone (HAZ) consists of a coarser granular bainitic structure with prior austenitic grain sizes of 43.09 and 16.93 μm for A-TIG and MP-TIG weld joints, respectively, as shown in Fig. 14(a) and (b).

The hardness profile of the cross section of the welded specimen measured at 3 mm from the top edge is shown in Fig. 15(a) and (b). As the hardness value is measured from the fusion boundary to base metal region, there is a drastic fall in

hardness value. At the weld center, the highest hardness value of around 320-350 (HV 0.3) was found in both A-TIG and MP-TIG weld joints. The hardness value of ~ 320 HV is a typical hardness level of bainite, which confirms the presence of bainitic microstructure. Base metal exhibited lower hardness due to normalized and tempered bainite. Moreover, MP-TIG weld joint showed inhomogeneity in microstructure and hardness profile than A-TIG weld joint. The corresponding variation in hardness profile is mainly due to the complex thermal cycle; i.e., the fresh pass reheats the previously deposited pass and tempers the region.

3.3 Mechanical Analysis

The strains produced by the thermal energy are coupled to mechanical analysis. The thermal strains and the volume strains produced due to solid-state phase transformation effect (especially in phase transformation steels) induce residual stress and distortion in the steel. The overall individual strain components can be expressed as shown in Eq 5.

Along with the strain factor, the change in the yield strength due to phase transformation affects the residual stress. Some of the researchers demonstrated the change in residual stress pattern with the comparison made by accounting and without considering the phase transformation effect; eventually, this showed an entirely different residual stress pattern (Ref 21). Hence, in the numerical model, it is necessary to include all the material properties for individual phases, especially the yield strength to get a reasonable result.

Figure 16(a) and (b) show the comparison between measured and predicted residual stress profiles for A-TIG and MP-TIG P22 weld joints. A sizeable longitudinal tensile residual stress accumulated in and around HAZ and weld zone due to hindered thermal contraction by the parent metal during cooling. The significant drop of welding residual stress is not observed in the fusion zone in spite of austenite-to-bainite phase transformation. In contrast, a decrease in stress level in the weld zone was generally observed in phase transformation steels. From the existing literature, it is well understood that P22 steels exhibit tensile residual stress at ambient temperature due to exhausted phase transformation relatively at a higher temperature (Ref 27, 28). Consequently, the reduced compensation of thermal strains by phase transformation strains will lead to raise the stress level and eventually tensile residual stress was observed in the weld joint due to shrinkage of the weld metal as shown in Fig. 17. Moreover, a study demonstrated the variation in residual stress at the weld zone as a

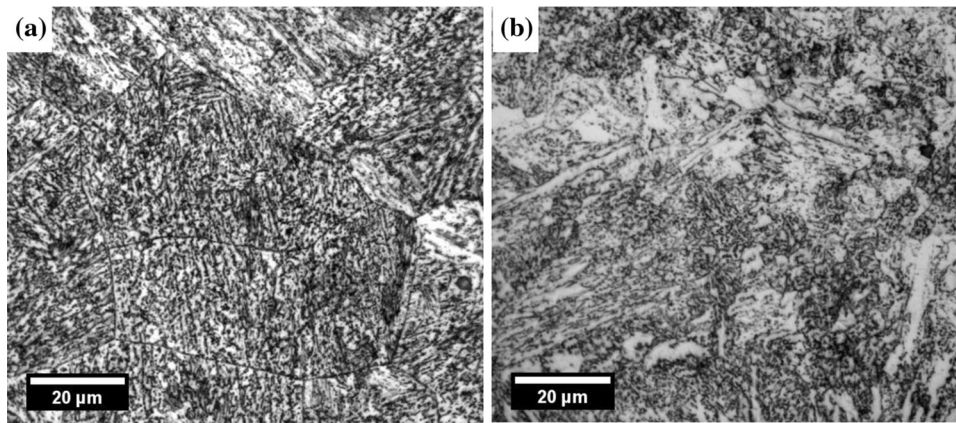


Fig. 13 Optical micrographs of weld metal (a) A-TIG and (b) MP-TIG weld joints

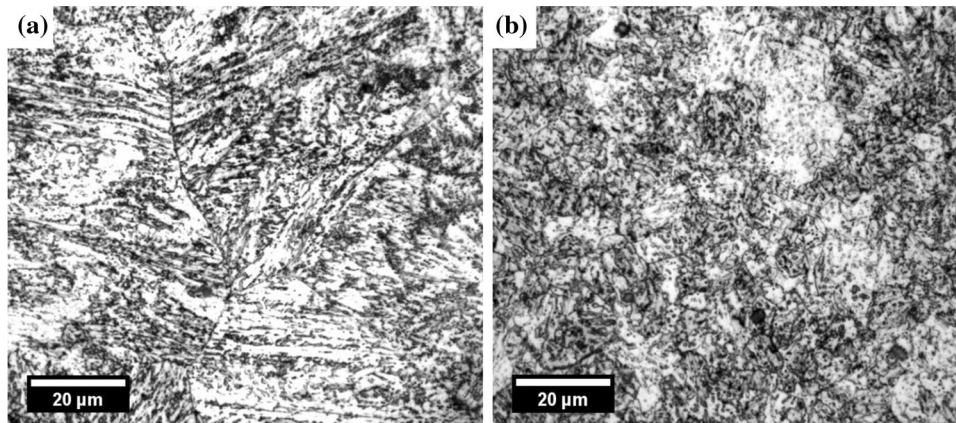


Fig. 14 Optical micrographs of HAZ (a) A-TIG and (b) MP-TIG weld joints

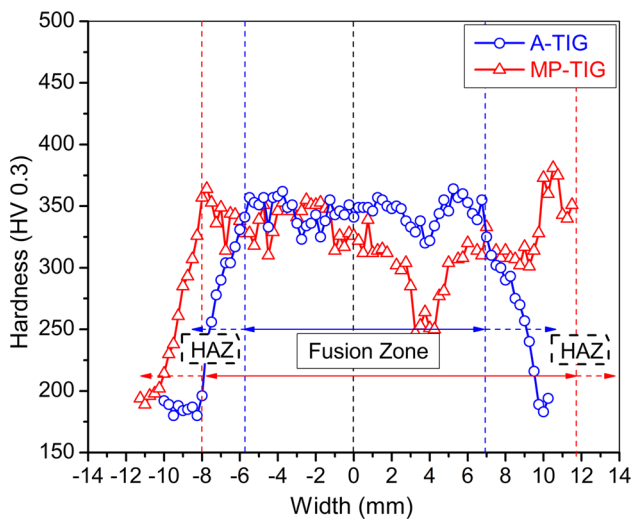


Fig. 15 Hardness comparison

function of phase transformation temperature. The study revealed that the magnitude of stress drop at the weld zone is dependent on the phase transformation start and finish temperature; i.e., the residual stress level decreased and became compressive as the transformation temperature decreased toward ambient temperature (Ref 29). Therefore, a small drop

in residual stress observed in the weld zone (Fig. 16a and b) can be attributed to phase transformation effect. Also, the internal stress balance may cause a drop in the magnitude of residual stress. The welding residual stresses in the previously deposited pass were modified by the subsequent weld pass due to the repeated thermal cycle of the welding process. The variation in the hardness value shows the effect of the final pass on the hardness value as shown in Fig. 15. Moreover, in welding, the deformation may occur when the residual stress exceeds the yield strength. The deformation will be minimal due to the external constraints; thus, there may be less strain hardening effect during welding. However, in MP-TIG weld joint, high level of distortion was observed than the A-TIG weld joint due to large weld metal volume. Lavanya et al. (Ref 30) showed that increased strain hardening reduced the level of residual stress in weld joints. Therefore, the drop in the magnitude of residual stress is prominent in MP-TIG weld joint. In the case of A-TIG welding process, measured peak tensile residual stress is 545 MPa while the predicted value was 619.2 MPa. In the case of the MP-TIG welding process, peak tensile residual stress of 594 MPa was measured while the model predicted 635.14 MPa. The peak tensile residual stress was observed in the HAZ for both the weld joints. This is due to the hindered shrinkage of the molten weld metal during solidification (Ref 12, 31). It is observed that the predicted result has the same trend as that of the experimental result. Figure 16(a) and (b) also shows the transverse residual stress

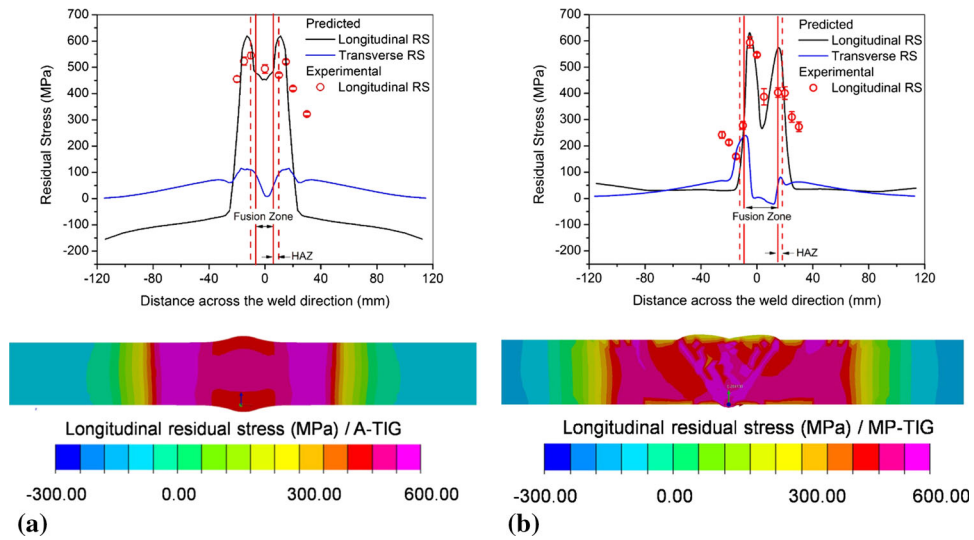


Fig. 16 Experimental validation and a mid-cross section of longitudinal residual stress (RS) across the (a) A-TIG and (b) MP-TIG weld joints

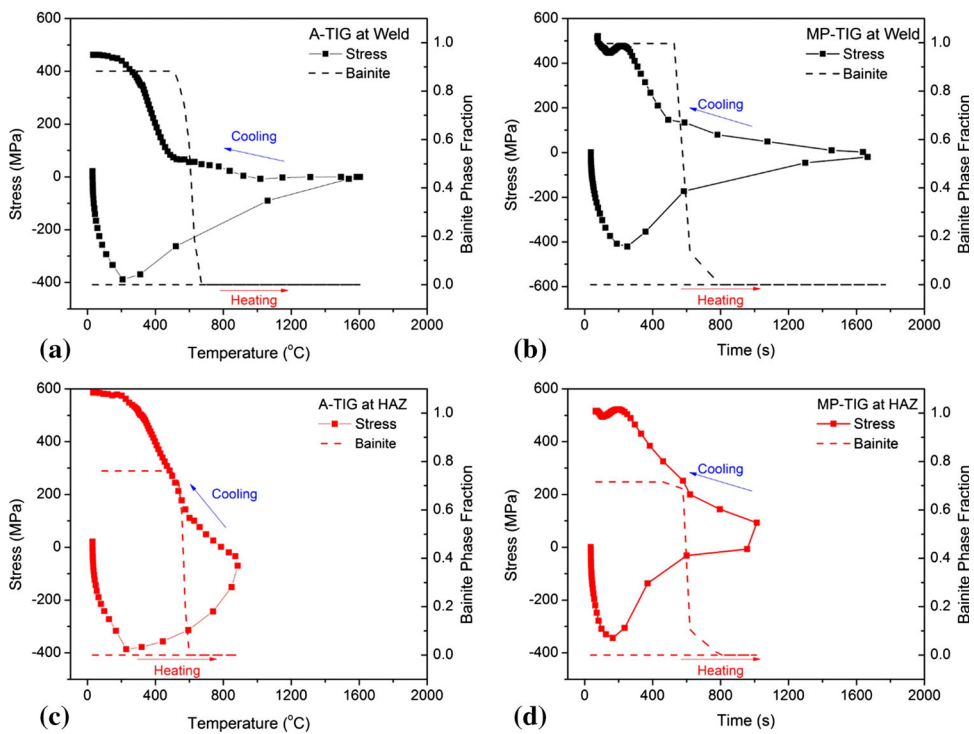


Fig. 17 Stress evolution as a function of temperature at a spot in weld joints of A-TIG and MP-TIG: (a) A-TIG at weld zone and (b) MP-TIG at weld zone. (c) A-TIG at HAZ and (d) MP-TIG at HAZ

distribution in A-TIG and MP-TIG weld joints. The predicted peak transverse residual stress was found to be 115 MPa and 240 MPa for A-TIG and MP-TIG weld joints, respectively. Predicted peak tensile residual stress values are higher in MP-TIG weld joints. Location of the peak stress in both the weld joints was in HAZ and close to the fusion boundary. Moreover, the significant difference in the peak value of transverse and longitudinal residual stress shows the domination of longitudinal residual stress in weld joints.

Figure 17 shows the generation of stress and formation of bainitic phase as a function of temperature at weld zone and HAZ during the first pass for A-TIG and MP-TIG weld joints,

respectively. The stress evolution for all welding passes is more complex; hence, only for the first pass, the stress evolution behavior is discussed in this paper. As the temperature starts to increase, the compressive residual stress starts to form and then it decreases to zero at the melting point. While cooling, due to dominating thermal strains, tensile stress increases. As the temperature decreases to 600 °C, the austenite-to-bainite phase transformation starts and depletes well above ambient temperature (~ 460 °C). It was observed from Fig. 17(a) and (b) that, in both cases, there was no obvious change in the residual stress pattern toward the compressive side due to phase transformation. At the temperature below ~ 460 °C, thermal strain dominates

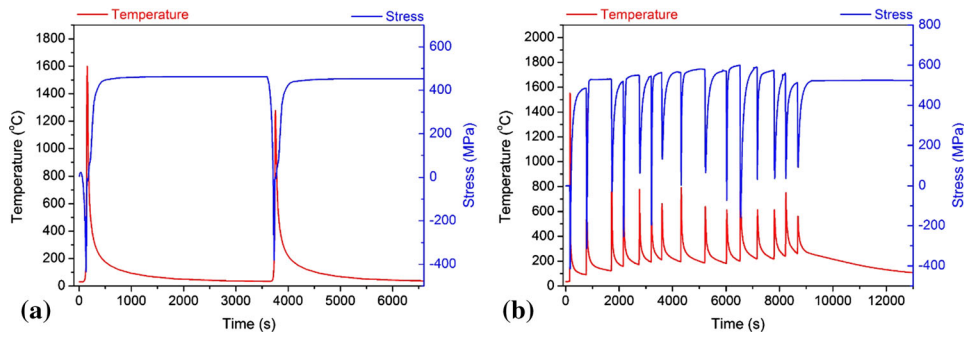


Fig. 18 Weld-induced residual stress: stress generation during welding at a spot in (a) A-TIG and (b) MP-TIG weld joints

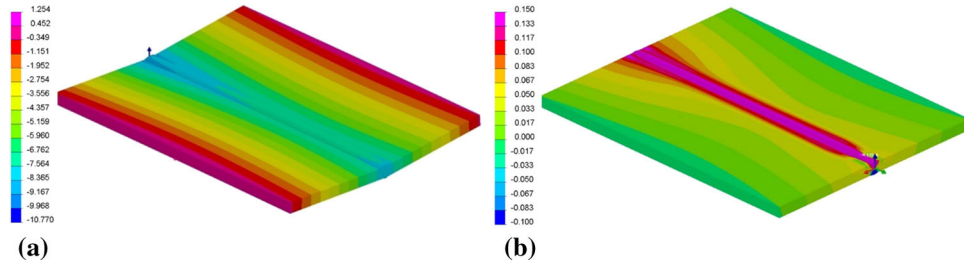


Fig. 19 Predicted distortion of (a) MP-TIG and (b) A-TIG weld joints

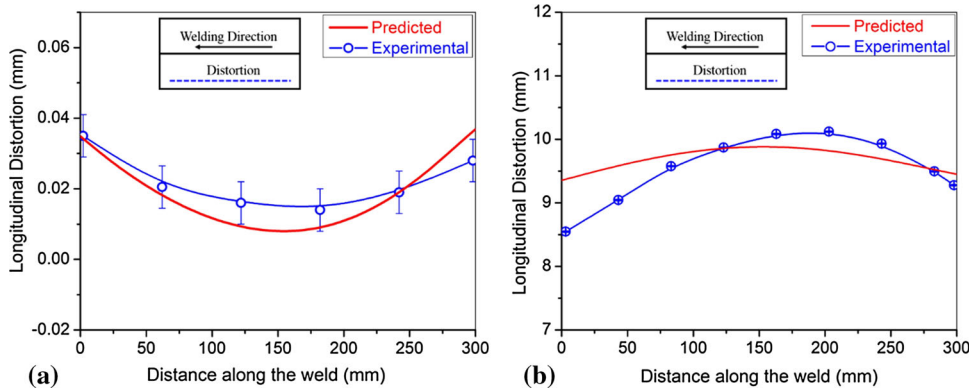


Fig. 20 Experimental validation of distortion: (a) A-TIG and (b) MP-TIG weld joints

the volume strain and eventually reaches the maximum value of the order of yield strength of the base/weld metal at ambient temperature. The high tensile residual stress is generated at the HAZ due to shrinkage of molten weld metal during solidification. The peak tensile residual stress eventually relies on the thermal contraction and not on the bainite phase proportion because the transformation is exhausting at a higher temperature. In addition, the difference in peak tensile residual stress between A-TIG and MP-TIG weld joints depends on the weld metal volume. The weld metal volume is relatively large in MP-TIG weld joint compared to A-TIG weld joint owing to the filler wire deposition over the v-groove. This, in turn, causes large shrinkage during cooling which results in very high residual stress and also distortion in the weld joint. Moreover, the evolution of stress during MP-TIG welding is more complex and influences the mechanical properties of the entire structure.

Figure 18(a) and (b) shows the stress generation during individual passes. This figure suggests that individual weld passes are responsible for the higher magnitude of residual stress and distortion in the weld joint. In MP-TIG weld joint, very complex stress profile in association with complex thermal cycle during welding shows the generation of tensile stress. At the end of each deposition, very high tensile stress was observed. The higher stress of the order of yield strength is mainly due to the large molten metal volume and shrinkage effect. Hence, the more distorted structure can be expected in MP-TIG weld joint compared to A-TIG weld joint.

The welded structure usually exhibits distortion due to improper use of external constraints or use of high heat input. The distortion is generated when the residual stress exceeds the yield strength of the materials resulting in plastic deformation which in turn causes distortion. From Fig. 19 and 20, it is clear

that the magnitude of distortion is more in case of MP-TIG weld joint compared to A-TIG weld joint.

The distortion of MP-TIG weld joint along the welding direction is shown in Fig. 20(b) and it was observed that the magnitude of the displacement was ~ 8.75 mm, whereas in A-TIG weld joint (Fig. 20a) the magnitude of displacement is negligibly small, which is ~ 0.03 mm. The filler metal deposition during MP-TIG process (15 weld passes) in v-groove configuration causes large shrinkage during cooling which results in very high distortion of the weld joint. Further, high depth-to-width ratio characterizing narrow weld bead and the symmetry of the weld metal predominately reduces the distortion in A-TIG weld joint. The predicted result showed reasonable agreement with the experimental results in both the weld joints.

4. Conclusions

1. Thermomechanical analysis has been carried out successfully employing SYSWELD for predicting thermal cycles, residual stresses and distortion in 11-mm-thick P22 steel weld joints during MP-TIG and A-TIG welding.
2. In case of double-pass A-TIG weld joint, the peak temperature remained constant for the entire weld length compared to MP-TIG weld joint. In MP-TIG weld joint, the peak temperature varied for individual passes. There was good agreement between the measured and predicted thermal cycles.
3. The magnitude of residual stress is relatively greater in MP-TIG weld joint (594 MPa) than A-TIG weld joint (545 MPa). Moreover, MP-TIG weld joint exhibited high distortion than A-TIG weld joint. This is attributed to more weld metal volume due to the v-groove configuration in MP-TIG weld joint causing more shrinkage. The predicted residual stress is consistent with the measured residual stress values. Distortion was much higher in MP-TIG weld joint than A-TIG weld joint. The predicted distortion values agreed with experimentally measured values.
4. Hardness and microstructure analysis indicated a significant amount of inhomogeneity in microstructure and hardness values in the case of MP-TIG weld joint. Similarly, the residual stress profile also exhibited sharp changes. A-TIG weld joint exhibited uniform hardness across the weld metal and so the residual stress distribution.
5. The comparative study with the help of thermomechanical analysis demonstrated that A-TIG welding process if employed, would reduce significantly the magnitude of distortion in 2.25Cr-1Mo steel weld joint compared to the MP-TIG welding process. Slight reduction in residual stress values was observed in A-TIG weld joint. Therefore, A-TIG welding is recommended for welding of 2.25Cr-1Mo steel.

References

1. A. Trautwein, H. Mayer, W. Gysel, and B. Walser, Structure and Mechanical Properties of 2¼Cr-1Mo Cast Steel for Pressure Compo-

- ponents with Wall Thicknesses up to 500 mm, in *Application of 2¼Cr-1Mo Steel for Thick-Wall Pressure Vessels*, ASTM International (1982)
2. K. Laha, K.B.S. Rao, and S. Mannan, Creep Behaviour of Post-weld Heat-Treated 2.25Cr-1Mo Ferritic Steel Base, *Weld Metal and Weldments, Mater. Sci. Eng., A*, 1990, **129**, p 183–195
3. B. Arivazhagan and M. Vasudevan, Studies on A-TIG Welding of 2.25Cr-1Mo (P22) Steel, *J. Manuf. Process.*, 2015, **18**, p 55–59
4. R. Kumar, V. Tewari, and S. Prakash, Studies on Hot Corrosion of the 2.25 Cr-1Mo Boiler Tube Steel and Its Weldments in the Molten Salt Na₂SO₄-60 pct V₂O₅ Environment, *Metall. Mater. Trans. A*, 2007, **38**, p 54–57
5. K. Mills, B. Keene, R. Brooks, and A. Shirali, Marangoni Effects in Welding, *Philos. Trans. R. Soc. Lond. Ser. A Math. Phys. Eng. Sci.*, 1998, **356**, p 911–926
6. M. Tanaka, T. Shimizu, T. Terasaki, M. Ushio, F. Koshiishi, and C.-L. Yang, Effects of Activating Flux on Arc Phenomena in Gas Tungsten Arc Welding, *Sci. Technol. Weld. Join.*, 2000, **5**, p 397–402
7. H. Fujii, T. Sato, S. Lu, and K. Nogi, Development of an Advanced A-TIG (AA-TIG) Welding Method by Control of Marangoni Convection, *Mater. Sci. Eng., A*, 2008, **495**, p 296–303
8. K. Ganesh, K. Balasubramanian, M. Vasudevan, P. Vasantharaja, and N. Chandrasekhar, Effect of Multipass TIG and Activated TIG Welding Process on the Thermo-Mechanical Behavior of 316LN Stainless Steel Weld Joints, *Metall. Mater. Trans. B*, 2016, **47**, p 1347–1362
9. M. Vasudevan, Effect of A-TIG Welding Process on the Weld Attributes of Type 304LN and 316LN Stainless Steels, *J. Mater. Eng. Perform.*, 2017, **26**, p 1325–1336
10. P.J. Withers and H. Bhadeshia, Residual Stress. Part 2–Nature and Origins, *Mater. Sci. Technol.*, 2001, **17**, p 366–375
11. R. Leggett, Residual Stresses in Welded Structures, *Int. J. Press. Vessels Pip.*, 2008, **85**, p 144–151
12. K. Masubuchi, *Analysis of Welded Structures: Residual Stresses, Distortion, and Their Consequences*, Elsevier, Amsterdam, 2013
13. J. Francis, H. Bhadeshia, and P. Withers, Welding Residual Stresses in Ferritic Power Plant Steels, *Mater. Sci. Technol.*, 2007, **23**, p 1009–1020
14. D. Deng and H. Murakawa, Finite Element Analysis of Temperature Field, Microstructure and Residual Stress in Multi-pass Butt-Welded 2.25Cr-1Mo Steel Pipes, *Comput. Mater. Sci.*, 2008, **43**, p 681–695
15. F. Vakili-Tahami, A. Daei-Sorkhabi, M. Saeimi-S, and A. Homayounfar, 3D Finite Element Analysis of the Residual Stresses in Butt-Welded Plates with Modeling of the Electrode-Movement, *J. Zhejiang Univ. Sci. A*, 2009, **10**, p 37–43
16. F. Vakili-Tahami and A. Sorkhabi, Finite Element Analysis of Thickness Effect on the Residual Stress in Butt-Welded 2.25 Cr1Mo Steel Plate, *J. Appl. Sci.*, 2009, **9**, p 1331–1337
17. D. Deng, Y. Tong, N. Ma, and H. Murakawa, Prediction of the Residual Welding Stress in 2.25 Cr-1Mo Steel by Taking into Account the Effect of the Solid-State Phase Transformations, *Acta Metall. Sin. (Engl. Lett.)*, 2013, **26**, p 333–339
18. Y. Zhou, X. Chen, Z. Fan, and S. Rao, Finite Element Modelling of Welding Residual Stress and Its Influence on Creep Behavior of a 2.25Cr-1Mo-0.25 V Steel Cylinder, *Procedia Eng.*, 2015, **130**, p 552–559
19. K. Ganesh, M. Vasudevan, K. Balasubramanian, P. Vasantharaja, and N. Chandrasekhar, Thermo-Mechanical Analysis of Activated Tungsten Inert Gas Welding (A-TIG) of Type 316LN Stainless Steel Thin Plates, *Mater. Perform. Charact.*, 2018, **7**, p 160–177
20. ESI Group *SYSWELD Reference Manual Version 2006*. Cedex, Paris, France, 2006
21. M. Zubairuddin, S. Albert, M. Vasudevan, S. Mahadevan, V. Chaudhari, and V. Suri, Numerical Simulation of Multi-pass GTA Welding of Grade 91 Steel, *J. Manuf. Process.*, 2017, **27**, p 87–97
22. J. Goldak, A. Chakravarti, and M. Bibby, A New Finite Element Model for Welding Heat Sources, *Metall. Trans. B*, 1984, **15**, p 299–305
23. T. Scott, G. Sangdahl, and M. Semchyshen, *Application of 2¼Cr-1Mo Steel for Thick-Wall Pressure Vessels*, American Society for Testing and Materials, STP755 (1982)
24. J. Leblond and J. Devaux, A New Kinetic Model for Anisothermal Metallurgical Transformations in Steels Including Effect of Austenite Grain Size, *Acta Metall.*, 1984, **32**, p 137–146
25. R. Klueh and R. Swindeman, *Mechanical Properties of a Modified 2¼ Cr-1Mo Steel for Pressure Vessel Applications*, No. ORNL-5995. Oak Ridge National Lab, TN, USA, 1983

26. M. Xu, H. Lu, C. Yu, J. Xu, and J. Chen, Finite Element Simulation of Butt Welded 2 25Cr-16 W Steel Pipe Incorporating Bainite Phase Transformation, *Sci. Technol. Weld. Join.*, 2013, **18**(3), p 184–190
27. W.K.C. Jones and P.J. Alberry, A Model for Stress Accumulation in Steels During Welding, *Met. Technol.*, 1977, **11**, p 557–566
28. H. Bhadeshia, Phase Transformations Contributing to the Properties of Modern Steels, *Bull. Pol. Acad. Sci. Tech. Sci.*, 2010, **58**(2), p 255–265
29. H. Murakawa, M. Beres, A. Vega, S. Rashed, C.M. Davies, D. Dye, and K.M. Nikbin, Effect of Phase Transformation Onset Temperature on Residual Stress in Welded Thin Steel Plates, *Trans. JWRI*, 2008, **37**(2), p 75–80
30. S. Lavanya, S. Mahadevan, and C. Mukhopadhyay, Correlation of Tensile Deformation-Induced Strain in HSLA Steel with Residual Stress Distribution, *J. Mater. Eng. Perform.*, 2019, **28**(2), p 1103–1111
31. R.W. Messler, *Principles of Welding: Processes, Physics, Chemistry, and Metallurgy*, Wiley, New York, 2008

Publisher's Note Springer Nature remains neutral with regard to jurisdictional claims in published maps and institutional affiliations.